Electro-mechanical behaviour of ferroelectrics: Insights into local contributions from macroscopic measurements

Valentin Segouin, Mathieu Domenjoud, Yves Bernard, Laurent Daniel

Acta Materialia 211 (2021) 116870

Contents lists available at ScienceDirect

Acta Materialia

journal homepage: www.elsevier.com/locate/actamat

Full length article

Electro-mechanical behaviour of ferroelectrics: Insights into local contributions from macroscopic measurements

Valentin Segouin[a,b], Mathieu Domenjoud[a,b], Yves Bernard[a,b], Laurent Daniel[a,b,*]

[a] Université Paris-Saclay, CentraleSupélec, CNRS, Laboratoire de Génie Electrique et Electronique de Paris, 91192, Gif-sur-Yvette, France
[b] Sorbonne Université, CNRS, Laboratoire de Génie Electrique et Electronique de Paris, 75252, Paris, France

ARTICLE INFO

Article history:
Received 11 June 2020
Revised 24 March 2021
Accepted 1 April 2021
Available online 7 April 2021

Keywords:
Digital image correlation
2D strain field
Hysteresis loops
Piezoelectric
Ferroelastic
Polarisation mechanisms

ABSTRACT

The behaviour of a bulk lead zirconate titanate ceramic has been characterised under combined high stress and high electric field. The electrical response of the sample was monitored, and Digital Image Correlation (DIC) was used to characterise the strain field at the surface of the sample. The DIC technique allows both longitudinal and transverse strains to be measured simultaneously. The results showed that a compressive stress of 25 MPa increases the susceptibility by 128% and the longitudinal piezoelectric coefficient by 47%. A further increase of stress has reversed this trend and under a 500 MPa compression, the susceptibility has fallen by 71% and the longitudinal piezoelectric coefficient by 98% compared to the unstressed case. The analysis of the ferroelastic contribution revealed that this decrease is explained by a saturation of the ferroelastic switching, beginning at the coercive field. The material volume change during loading was computed using the DIC results. It was found that a negligible piezoelectric activity remains at 500 MPa while ferroelastic switching still occurs and is reversible. This work shows that it is possible to obtain quantitative insights into the physical mechanisms underlying the macroscopic behaviour of ferroelectrics using the DIC technique without requiring the use of local investigation technique.

1. Introduction

Ferroelectric materials are widely used to produce actuation systems such as traveling wave motors [1–3], structural resonance motors [4–6], walking [7] or clamping systems [8,9], inertial motors [10] or meshing engagement motors [11]. In all these actuation mechanisms, the ferroelectric material is simultaneously subjected to an electric field and a mechanical stress. A full understanding of ferroelectric materials behaviour under such conditions is required to optimise these devices.

Several studies were conducted to observe [12–14] and model [15–21] the macroscopic behaviour of soft ferroelectric materials under coupled electromechanical loadings. However, boundary conditions are difficult to control and experimental studies are usually restricted to low stress [22–24] ($<$ 60 MPa) or subcoercive electric field [22,25,26]. Studies where stress and electric field both largely overtake the coercive values of the material can be found [27–33], but only a few include piezoelectric and ferroelastic properties measurements [31–33]. Similarly the measurement of the transverse strain under high field and high stress was already investigated [34] but is still rarely shown. To facilitate a complete investigation of the material behaviour under severe electromechanical loadings, new investigation techniques are needed.

Digital Image Correlation (DIC) is a computation technique used to extract the 2D displacement field between two images of the same scene. It has been used to study the strain field of structural materials during classical mechanical tests such as tensile, compression, shear, torsion and bending [35–39]. Severe conditions were also studied such as high temperature [40], large strains [41,42] or high strain rates [43,44]. Over the past six years, DIC has been introduced for the study of ferroelectric material response to external loadings [45–49]. The ferroelastic strain was studied either under electric field [[45–47],[49]] or mechanical stress [48]. Piezoelectric properties were also studied [45,49]. In [49], it was shown that DIC can give access to electric-induced strains down to 3×10^{-6} and allows defining piezoelectric coefficients of the or-

* Corresponding auhtor at: Université Paris-Saclay, CentraleSupélec, CNRS, Laboratoire de Génie Electrique et Electronique de Paris, 91192, Gif-sur-Yvette, France.
E-mail address: laurent.daniel@centralesupelec.fr (L. Daniel).

https://doi.org/10.1016/j.actamat.2021.116870

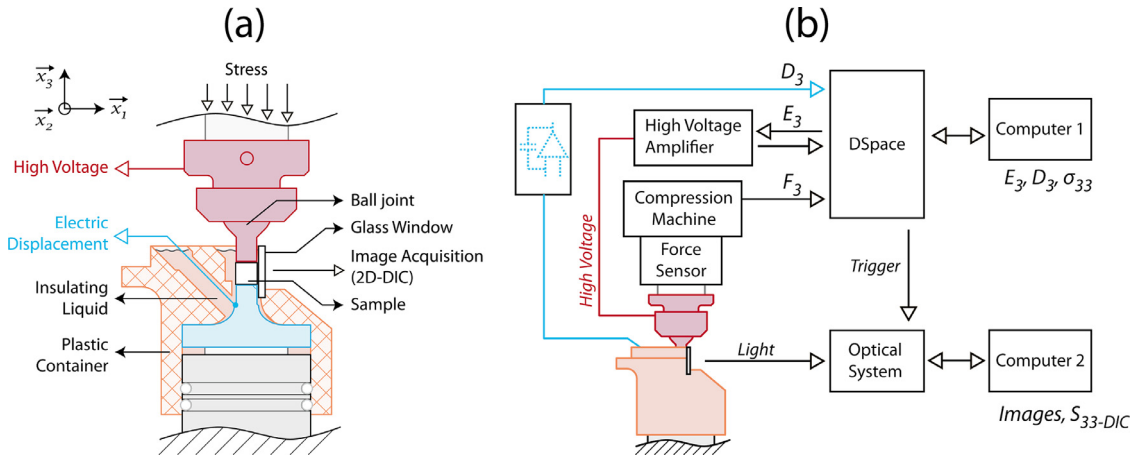

Fig. 1. Drawing of the loading cell (a) and illustration of the whole experimental setup (b). (For interpretation of the references to color in this figure legend, the reader is referred to the web version of this article.)

der of 20 pm/V. Besides, unlike classical strain measurement techniques, DIC does not only provide the average strain response of the material but the full displacement field over the studied area. This can be very useful as a mean to monitor the test conditions [[47–49]].

In the present work, DIC is used to study the properties of a soft lead zirconate titanate (PZT) ceramic under combined electrical and mechanical loading. The experimental setup and the measurement procedure are described in a first part. The classical *P-E* and *S-E* loops obtained for different levels of applied pre-stress are presented. Ferroelectric, piezoelectric and dielectric properties are then evaluated as a function of stress and electric field. The different contributions to the material behaviour (ferroelectric, ferroelastic, elastic, dielectric and piezoelectric) are further extracted from the results and discussed. It is shown that DIC measurements can be used to associate changes in material properties to specific micro-mechanical phenomena such as domain switching or crystal phase transitions.

2. Experimental procedures

2.1. Measurement setup

The electromechanical compression setup is shown in Fig. 1a. The setup is designed to apply to the sample an electric field E_3 up to 4 kV/mm and a force F_3 up to 10 kN (corresponding to a stress σ_{33} up to 600 MPa). The sample is a 4 × 4 × 4 mm soft PZT (NCE55, Noliac) with silver electrodes. The material, initially isotropic after sintering, was subjected only to uniaxial electromechanical loading along direction 3, so that it is assumed transverse isotropic around axis 3. The sample is placed between two jaws, electrically isolated from the ground using alumina parts. The upper jaw (red parts) contains a ball-joint and is used to apply the high voltage. The lower jaw (blue part) is used to measure the induced electric displacement D_3. All bearing surfaces were grinded and have a flatness within ± 4 µm.

The complete experimental setup is shown in Fig. 1b. The electric field E_3 is produced by a Trek 20/20C HS high voltage amplifier. For insulation purpose, the sample is immersed into a plastic container filled with insulating fluid (Fluorinert™ FC-770, 3M). The electric displacement D_3 is measured using an operational amplifier integrator circuit [50,51]. The integrating capacitor is of 2 µF. The force is applied by a Zwick/Roell 030 compression machine and is measured by a 10 kN sensor (KAP-TC, Angewandte System Technik), mounted between the machine loading frame and the upper jaw. The force and the electric field are collinear. A real-time dSPACE hardware module is used to apply E_3 and acquire F_3 and D_3. The module has a maximum sampling frequency of 50 kHz and is controlled from a computer using a real-time Graphical User Interface.

The in-plane strain field is measured by Digital Image Correlation [49]. A speckle pattern is deposited on a lateral face of the sample so as to track local displacements [52]. The deposition process is described in [49]. The speckled face is imaged during experiments with a Ximea MD091MU-SY camera mounted on a Questar QM100 MKIII. This optical setup is placed at ~37 cm from the sample surface. It can acquire 3380 × 2708 px size images at a maximum rate of 5 Hz, with a spatial sampling of ~1.2 µm/px (area of ~3.2 × 4 mm). A flat glass window (1 mm thick) mounted on a side of the plastic container (see Fig. 1a and 1b) allows a visual access to the sample. A minimum distance of 0.8 mm between the sample and the glass ensures that no contact appears during the experiment. The sample lighting is produced by a LLS 3 LED light source (SCHOTT North America, Inc.) and oriented with an optical fibre. The camera is triggered by the dSPACE module to synchronise the image acquisition with the applied electric field. A second computer is used to store the images. The in-plane displacements are obtained from the images using a Digital Image Correlation program based on a global approach (CorreliRT3) [49,53]. The strain field is computed from the displacement field using a finite-element algorithm. A mesh with triangular elements of 64 px is used for this purpose. More details on the optical setup and on the DIC program are given in [49].

2.2. Measurement procedure

Polarisation P_3, longitudinal strain S_{33} and transverse strain S_{11} were all measured simultaneously. The stress levels ranged from 2 to 500 MPa (compressive stresses will be noted positive). During the experiment, the system controlled the stress so that it did not vary by more than ± 6 MPa. The loading stress rate to reach each pre-stress level was 0.63 MPa/s. The electric field was triangular, with amplitude ± 4000 V/mm and frequency 25 mHz. The image acquisition frequency was set to 5 Hz so as to obtain 200 points for each *S-E* loop. To take into account the time-dependency of depolarisation under constant stress [54,55], the stress was maintained 100 s before electric field was started. For each stress level, four electric field cycles were applied to stabilise the sample response. Only the last cycle was recorded. The reference state for all strain values is chosen at $E_3 = 0$ and $\sigma_{33} = 2$ MPa. In the following, the remanent strain will refer to the strain measured between the reference state and the remanent state ($E_3 = 0$ at any σ_{33}).

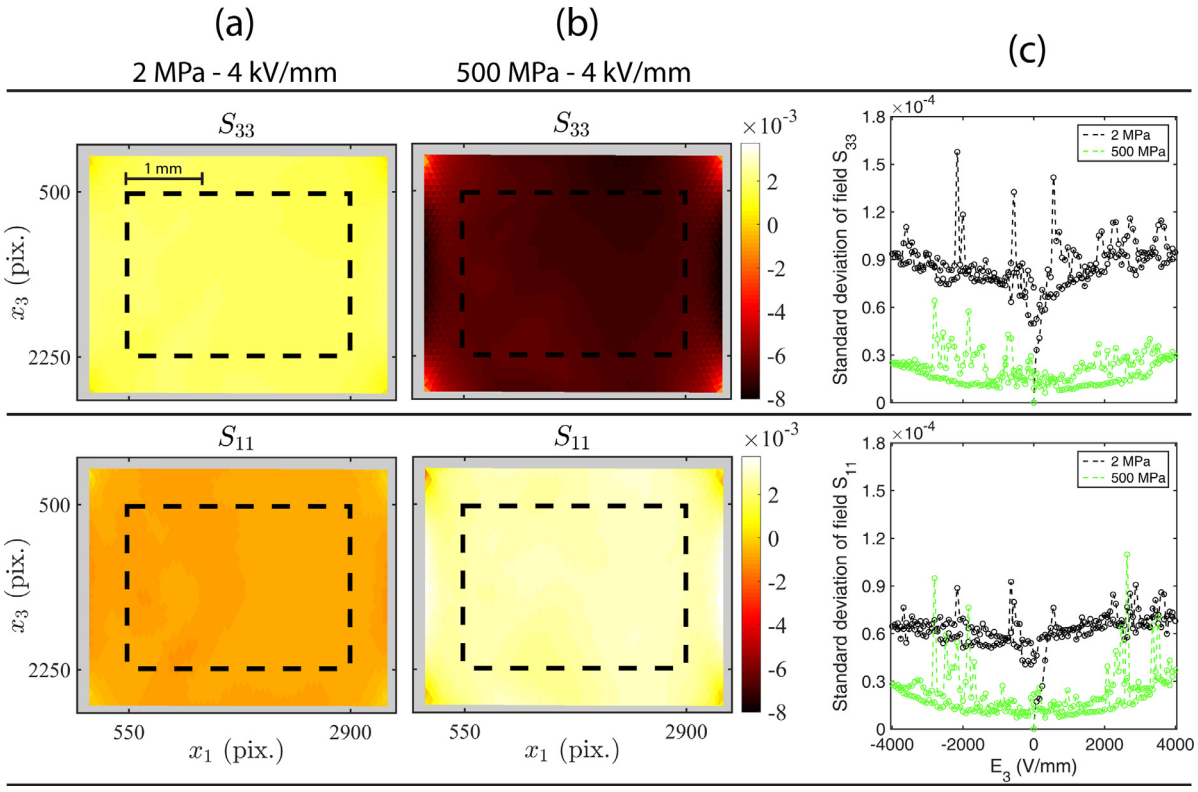

Fig. 2. Longitudinal (S_{33}) and transverse (S_{11}) DIC strain fields at (2 MPa, 4 kV/mm) (a) and at (500 MPa, 4 kV/mm) (b). Standard deviations of the strain fields S_{33} and S_{11} as a function of the electric field for 2 MPa (black curve) and 500 MPa (green curve) (c). The reference state for fields in (a) and (b) is the material state at 0 V/mm and 2 MPa. (For interpretation of the references to color in this figure legend, the reader is referred to the web version of this article.)

Fig. 2a shows S_{33} and S_{11} strain fields obtained under 2 MPa and 4 kV/mm. The coloured areas are the Region Of Interest (ROI). The grey parts thus represent uncorrelated pixels and show no data. The black dashed rectangles represent the zone within which the mean and standard deviation of the field are computed. This zone contains 1982 elements. The borders are discarded to exclude possible correlation errors associated with edge effects [49]. At 2 MPa and 4 kV/mm, the mean S_{33} value is 1.82 $\times$ 10^{-3}, the mean S_{11} is -0.85 $\times$ 10-^{3} and their respective standard deviations - calculated from the value of strain on the 1982 elements - are 9.5 $\times$ 10^{-5} and 6.8 $\times$ 10^{-5}. The standard deviations are less than 6% of the mean S_{33} value. The strain fields are thus satisfyingly homogeneous. This observation is important as clamping stresses can significantly affect the material strain within 3 mm of the bearing surface [48].

The shear strain S_{31} is not shown since its mean value does not exceed 2% of the mean S_{33} value. Fig. 2b similarly presents S_{33} and S_{11} strain fields under 500 MPa and 4 kV/mm. It can be seen that the strain field remains homogeneous with mean values -6.86 $\times$ 10^{-3} for S_{33} and 2.79 $\times$ 10^{-3} for S_{11}. Standard deviations - on the mean value - are of the order of 3 $\times$ 10^{-5}.

The strain field was similarly analysed for other applied electric fields between -4 and 4 kV/mm. The corresponding standard deviations are shown in Fig. 2c as a function of the electric field, for 2 and 500 MPa pre-stress levels. The curves exhibit local peaks, presumably due to experimental errors. One possible explanation is the presence of out of plane motions [56]. Such effect was not observed on previous stress-free experiments [46,47,49] and are thus possibly induced by the compression machine under force-control condition. The heterogeneity of the strain field is however acceptable, with a standard deviation below 1.6 $\times$ 10^{-4}. Such value represents a contribution of 3.6 $\times$ 10^{-6} to the total experimental error on the mean strain, which is about 3 $\times$ 10^{-5}.

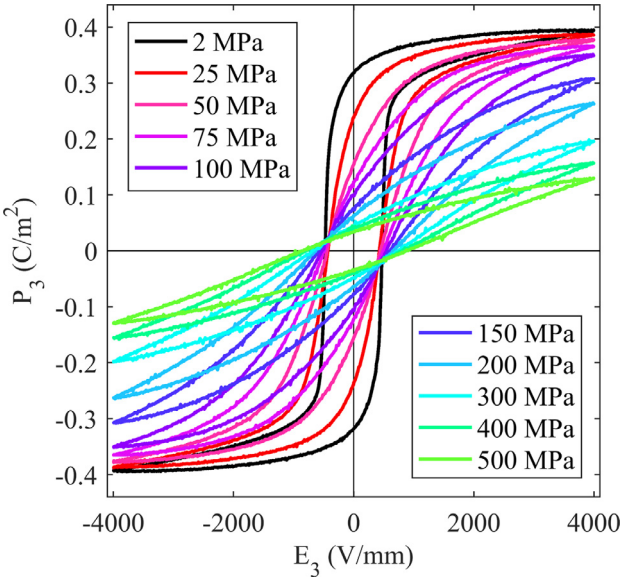

Fig. 3. *P-E* loop measured on NCE55 for different levels of uniaxial static compressive pre-stress. (For interpretation of the references to color in this figure legend, the reader is referred to the web version of this article.)

3. Results

Fig. 3 shows the *P-E* hysteresis loops under different compressive stress levels. The polarisation amplitude decreases with an increasing stress. The slope of the curve at the coercive field also decreases and the *P-E* loop consequently slants. Its shape goes from squared at 2 MPa to a stretched rhombus at 500 MPa. These ob-

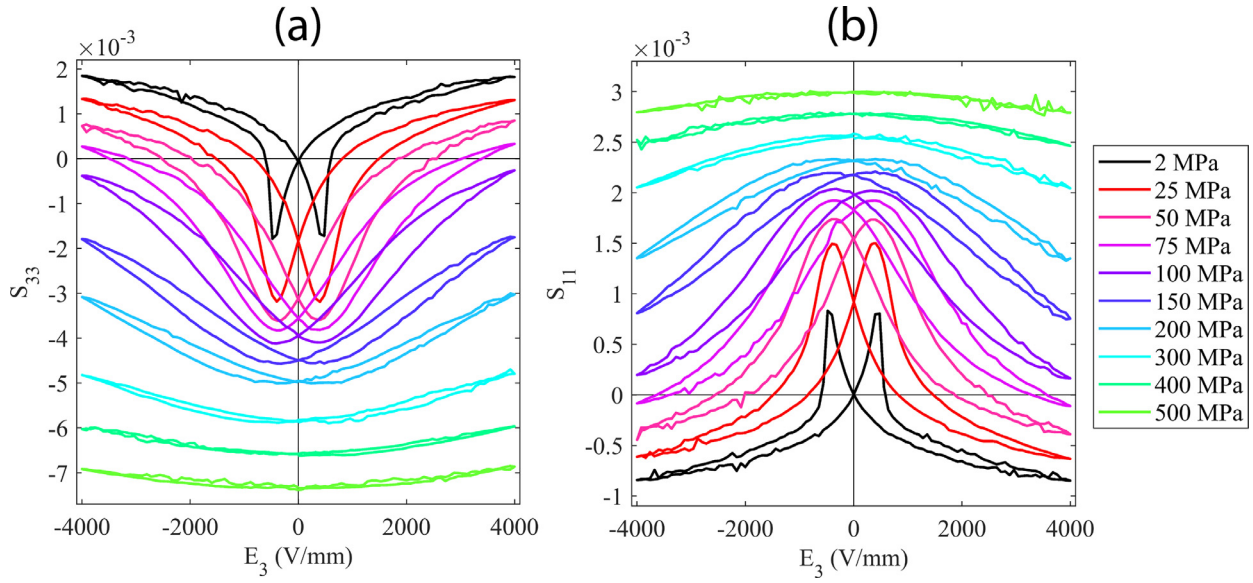

Fig. 4. Longitudinal (a) and transverse (b) *S-E* loops measured on NCE55 for different levels of static compressive pre-stress. (For interpretation of the references to color in this figure legend, the reader is referred to the web version of this article.)

servations are classical for PZT based ceramics [23,27,31,57]. The remanent polarisation P_r first drastically decreases until 300 MPa. Beyond this stress value, the reduction of P_r is limited as the material state tends to a mechanically saturated state.

Similarly to the polarisation amplitude, the strain amplitude decreases with the increase of the compressive stress (Fig. 4a and b). The remanent S_{33} (or S_{11}) and the minimum S_{33} (or maximum S_{11}) converge toward each other. The *S-E* loop area decreases as stress increases and, contrary to the *P-E* area, it becomes negligible above 300 MPa. These results are consistent with previous observations on similar materials [23,31,58]. The *S-E* loops contain local strain peaks with an amplitude up to 10^{-4} (see Fig. 4a and b – for instance at 2 MPa, around -2 kV/mm). The position of these peaks matches those seen on the strain standard deviation in Fig. 2c. As explained in the previous section, it is believed that these anomalies are caused by measurement errors.

4. Discussion

The results shown in the previous section are used to study the effect of stress on ferroelectric, dielectric and piezoelectric properties. They are further used to separate the piezoelectric, elastic and ferroelastic contributions from the material behaviour. In order to improve the clarity of the discussion, a review of the main contributions to ferroelectric behaviour is introduced in a first part. The second part shows the evolution of the ferroelectric, piezoelectric and dielectric properties as a function of stress and electric field. The third and fourth parts are focused on the ferroelastic contribution and the material volume variation.

4.1. Review of the main contributions

In ferroelectrics, the polarisation and strain changes under external loading (such as electric field or stress) are produced by several mechanisms among which ferroelasticity, elasticity, piezoelectricity, dielectricity and ferroelectricity play a major role [12,14,26]. Microstructural effects are commonly distinguished from local effects. Ferroelasticity and ferroelectricity - associated with an evolution of the domain microstructure - are referred to as extrinsic effects. Elasticity, piezoelectricity and dielectricity are called intrinsic contributions [59–61]. The characteristics of these contributions are schematically illustrated in Fig. 5.

Ferroelasticity and ferroelectricity refer to the possible reorientation of the spontaneous strain and polarisation of a crystal under stress or electric field (see Fig. 5, local scale) [23]. Both effects are associated with domain switching through 180° and non-180° domain wall motions (see Fig. 5, global scale). These contributions saturate at high external fields, are non-linear and dissipative. Importantly, changes in polarisation can be induced by 180° and non-180° wall motions whereas changes in strain are only induced by non-180° wall motions [62–65].

Elasticity is the reversible stress-strain distortion of the crystal lattice and is characterised by Hooke's law (Fig. 5, local scale). This phenomenon only affects the material strain and adds up to the ferroelastic behaviour [66]. Since the stiffness of a single crystal is anisotropic, the overall stiffness at the polycrystal scale depends on the orientation distribution of the single crystals within the material.

Dielectricity is the reversible electric field induced polarisation observed in non-conductive materials [68]. The physical mechanism causing this polarisation may either be electronic, ionic, dipolar or interfacial. At the local scale, the $P(E)$ relation is generally linear (see Fig. 5, local scale). At the polycrystal scale, this relation remains linear as long as no ferroelectric switching occurs. During ferroelectric switching, changes in permittivity appear due to the reorientation of the spontaneous polarisation (see Fig. 5, global scale).

Piezoelectricity [69] arises from charges anisotropy in noncentrosymmetric crystal structures. Each unit cell polarises under non-hydrostatic stress and deforms under electric field. Similarly to the dielectric response, the amplitude of the piezoelectric response depends on the angle of the applied field toward the spontaneous polarisation of the crystal. The piezoelectric contribution thus also relies on the crystal orientation and on domain configuration. At the polycrystal scale, the relations $P(\sigma)$ and $S(E)$ can be taken as linear but the linearity coefficients (d_{ij}) change with domain switching (see Fig. 5, global scale).

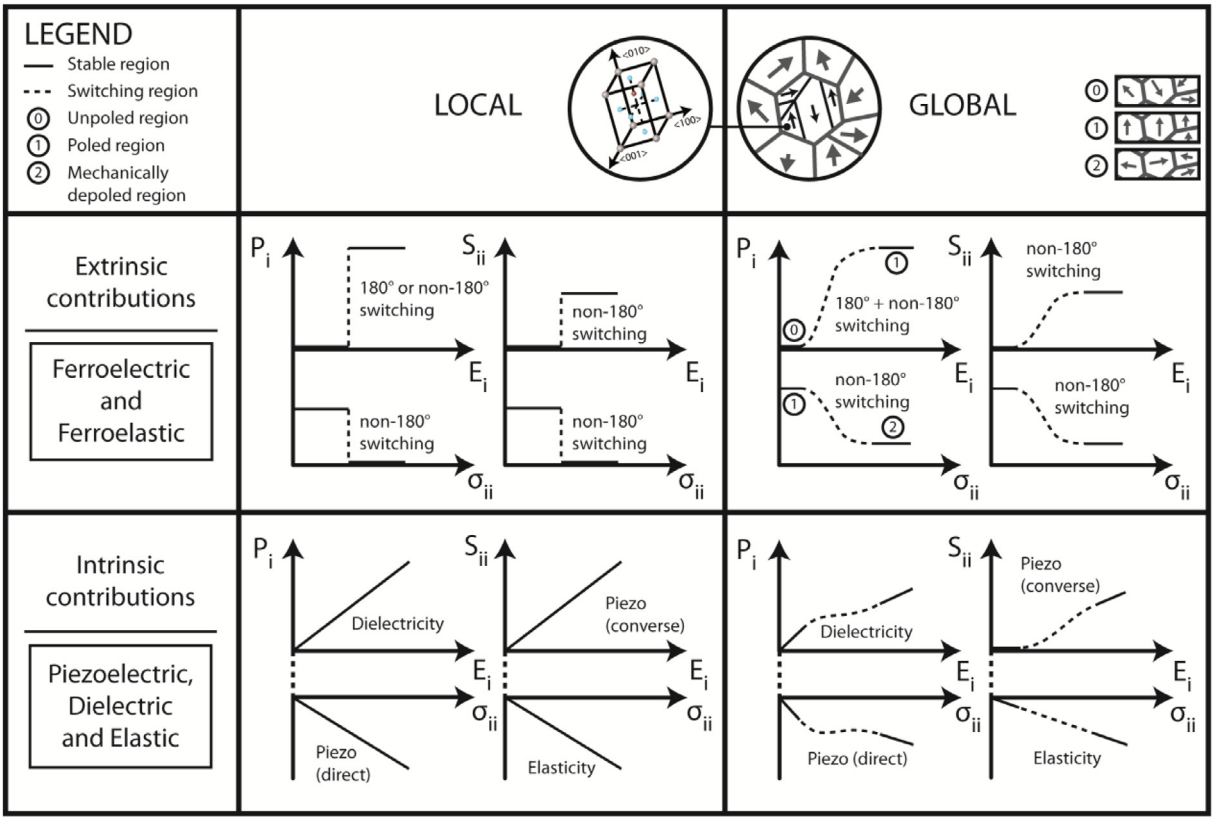

Fig. 5. Illustration of the ferroelectric, ferroelastic, piezoelectric, dielectric and elastic contributions at the crystal lattice scale (local) and at the polycrystal scale (global). At the local scale, the contributions are independent of each other. At the global scale, the total amplitude of each contribution depends on the crystal orientation distribution (anisotropy). The piezoelectric and dielectric contributions further depend on the ferroelectric switching [67]. They are affected by the direction of the spontaneous polarisation with respect to the applied electric field or the normal stress.

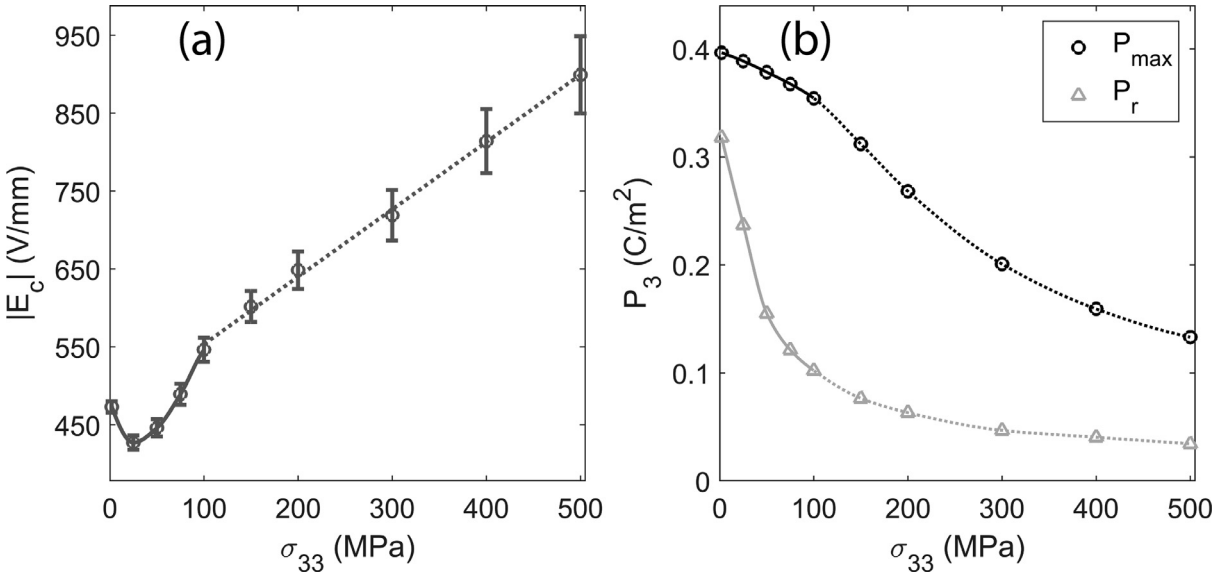

Fig. 6. Ferroelectric properties: Coercive field E_c (a), maximum polarisation P_{max} and remanent polarisation P_r (b). Values are obtained from Fig. 3. E_c is estimated by linear regression around $P_3 = 0$. The error bar represents the error propagated from P_3 by the linear regression.

4.2. Ferroelectric, piezoelectric and dielectric properties

Fig. 6a and 6b show the coercive field absolute value $|E_c|$, the remanent polarisation P_r and the maximum polarisation P_{max} as a function of the compressive stress. These parameters were obtained from the *P*-*E* loops of Fig. 3. P_{max} was obtained at maximum electric field. $|E_c|$ and P_r were obtained using a local linear regression of the *P*-*E* loop such that $P(E_c) = 0$ and $P_r = P(E = 0)$. Values obtained for positive and negative electric fields are averaged.

If we look at the coercive field evolution (Fig. 6a), the general tendency (evident above 100 MPa) is that stress tends to increase - almost linearly - the coercive field, as the microstructure evolves toward a mechanically saturated state. The increase rate is approximately 0.18 %/MPa, calculated between 100 and 500 MPa and tak-

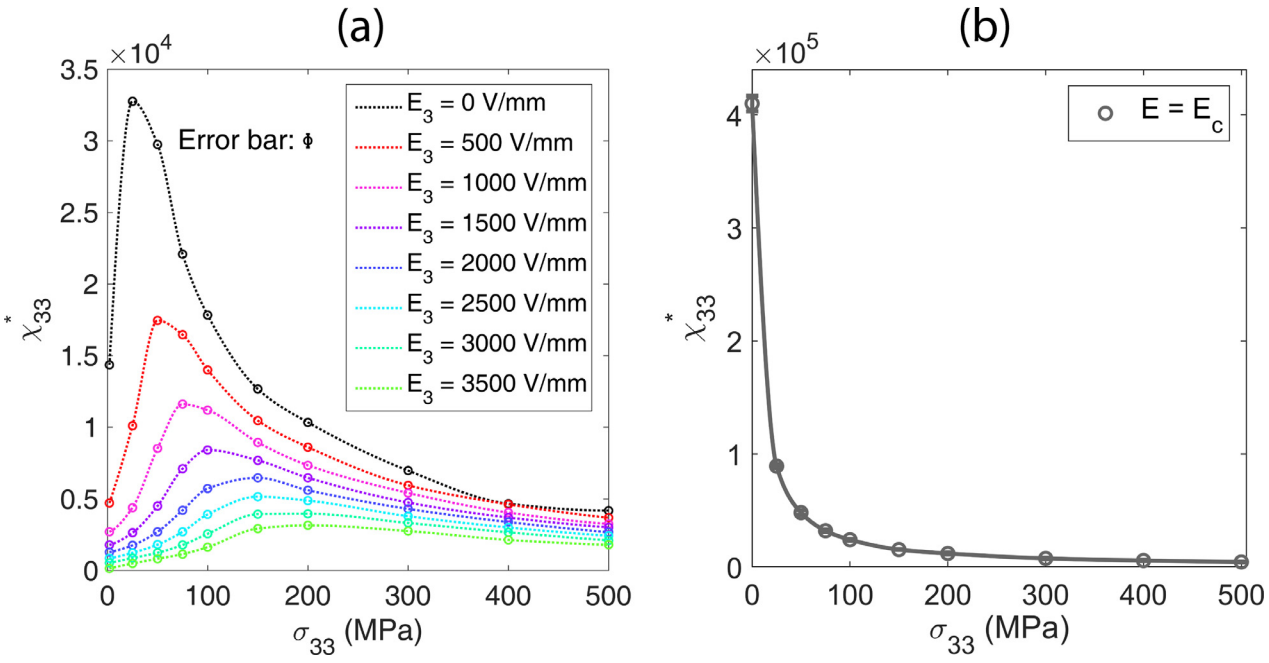

Fig. 7. Apparent susceptibility χ_{33}^* as a function of the compressive stress obtained in the poled region (when E decreases from E_{max} to 0) (a) and obtained at $E = E_c$ (b). χ_{33}^* is obtained from Fig. 3 by local linear regressions of the *P-E* loops. The regressions are computed within a window of 20 to 60 points, corresponding to 1.6 – 4.8% of the electric field period. Values of χ_{33}^* obtained for negative and positive regions are averaged. The error bar represents the error propagated from P_3 by the linear regression. (For interpretation of the references to color in this figure legend, the reader is referred to the web version of this article.)

ing the reference at 2 MPa. In the literature, various results are found: $|E_c|$ either increases or decreases [28,33,70] and its relative variation ranges from 0.02 %/MPa to 2.5 %/MPa [33,71,72]. Here, the increase of $|E_c|$ means that the mobility of walls is impeded by the application of stress. This can be interpreted as a consequence of the refinement of the domain structure due to stress, which increases the number of domains, and hence the number of walls. The defects of the material are then more likely to be active as a block to wall mobility. At low stress (below 100 MPa), a deviation from this linear increase of $|E_c|$ is observed, and an additional and opposite contribution seems to emerge, resulting in a drop of the coercive field. This is interpreted as a promotion of domain wall mobility in that region. Since stress does not significantly affect 180° wall mobility, the conclusion is that low stresses favour non-180° wall mobility, in the region of the coercive field.

If we now look at the remanent polarisation P_r (Fig. 6b), a sharp drop is observed at low stress levels (-75% in the range 2-100 MPa). The maximum polarisation P_{max} also drops down, but to a lesser extent (-11%). The order of magnitude of these variations is consistent with previous studies [27,28]. This shows a decrease in the activity of 180° switching in the region from the coercive field to saturation. A good indicator of the wall mobility in the remanence region is the difference between maximum and remanent polarisation, which indicates the degree of reversibility of the material polarisation. It is clear from Fig. 6b that this degree of reversibility first increases with stress (below 100 MPa) and then decreases. Again, it is assumed that stress is mostly effective on non-180° wall motions, so that in this region non-180° domain walls mobility is favoured.

This observation is consistent with the evolution of both susceptibility and piezoelectric coefficients at low stress, shown hereafter in Figs. 7 and 8. The apparent susceptibility χ_{33}^* (Fig. 7a) and the apparent piezoelectric coefficients d_{33}^* and d_{31}^* (Fig. 8a and 8b) were calculated from the *P-E* loops of Fig. 3 and the *S-E* loops of Fig. 4, respectively. Only the regions where the material is poled are represented (i.e. from P_r to P_{max}, excluding switching regions). The evolution of the susceptibility χ_{33}^* in the switching region is specifically shown in Fig. 7b. These properties are computed as partial derivatives ($\chi_{33}^* = \frac{\partial P_3}{\partial E_3}$; $d_{33}^* = \frac{\partial S_{33}}{\partial E_3}$; $d_{31}^* = \frac{\partial S_{11}}{\partial E_3}$). Values for positive and negative electric fields were averaged. The obtained parameters are called “apparent” because the extrinsic contribution remains significant [12,26,73].

If we look at the susceptibility at the remanence, when $E_3 = 0$, (black curve, Fig. 7a), a peak is observed in the first region (at $\sigma_{33} = 25$ MPa). A similar peak was observed at 50 MPa on another soft PZT [32], using unipolar *P-E* loops ($0 \leq E_3 \leq 2000$ V/mm). In the present case, the relative χ_{33}^* variation from 2 MPa reaches +128% at 25 MPa and then decreases down to -71% at 500 MPa. The χ_{33}^* peak at 25 MPa is linked to the increase of domain walls mobility, deduced previously from Fig. 6. At the left of the peak ($\sigma_{33} \approx 0$), the stress is too low to contribute significantly to the equilibrium compared to the contribution of the electric field. At the right of the peak, the stress saturates the fraction of non-180° domains ($\sigma_{33} > 100$ MPa). Regarding the electric field dependency, the susceptibility decreases as E_3 increases since the material polarisation reaches the electrical saturation. However, near the coercive field, the susceptibility seems to decrease monotonically with the applied stress (see Fig. 7b). This is consistent with the previous observations as it suggests that 180° wall mobility is not particularly favoured by the application of stress, contrarily to non-180° wall mobility at low stress.

The apparent piezoelectric coefficients d_{33}^* and d_{31}^* are shown in Fig. 8a and 8b. Since non-180° domain walls motion affects both polarisation and strain, the piezoelectric properties also exhibit a peak within the 2-100 MPa stress range. The d_{33}^* variation (from 2 MPa) reaches +47% at 25 MPa and -98.5% at 500 MPa. The d_{33}^* variation at 25 MPa is 2.7 times lower than the variation of χ_{33}^*. This is attributed to the fact that some non-180° wall motions can cancel their contribution to the material strain. Considering a domain whose orientation is opposite to that of the electric field, two successive non-180° reversals will lead to zero strain but will be associated with an increase in polarisation.

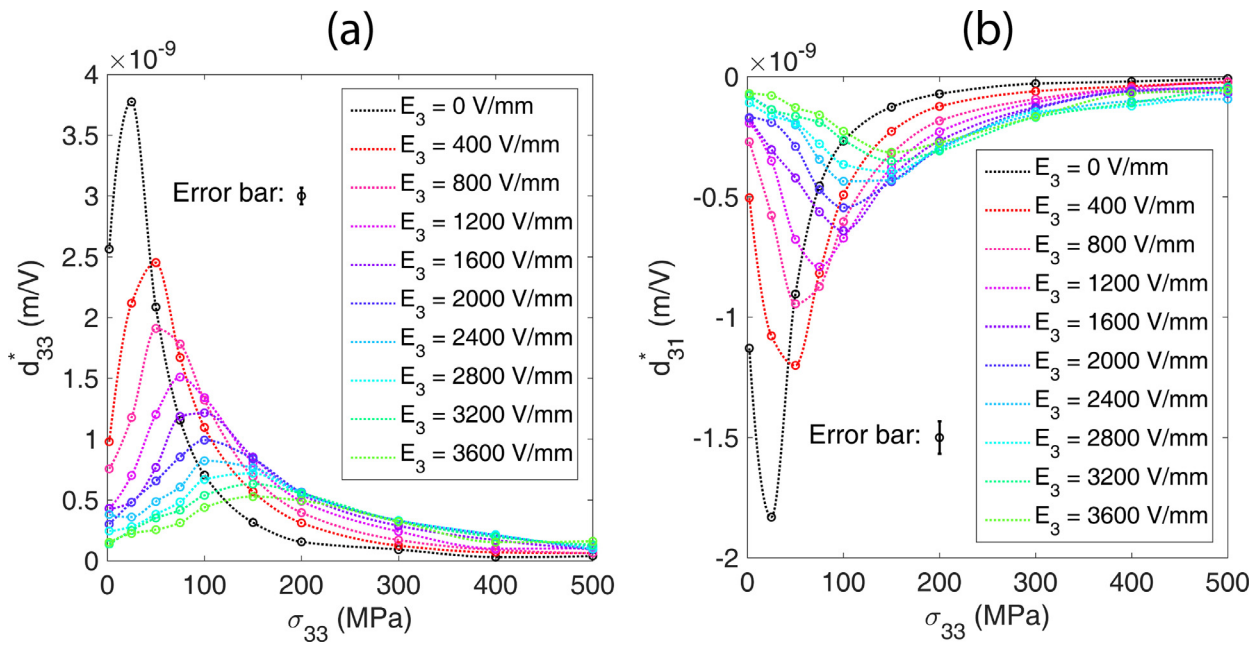

Fig. 8. Apparent piezoelectric coefficients d^*_{33} (a) and d^*_{31} (b) as a function of the compressive stress and for different applied electric fields, in the poled region (when E decreases from E_{max} to 0). The coefficients are obtained from Fig. 4 by local linear regressions of the S-E loops. The regressions are computed within a window of 4 to 22 points, corresponding to 2 – 11% of the electric field period. Coefficients obtained for negative and positive saturating regions are averaged. The error bar represents the error propagated from S_{33} and S_{31} by the linear regression. (For interpretation of the references to color in this figure legend, the reader is referred to the web version of this article.)

It is also worth noting that the decrease of d^*_{33} and d^*_{31} observed for high stress is more significant and abrupt than the decrease of χ^*_{33}. It is presumably because 180° wall motions still contribute to χ^*_{33} while d^*_{33} and d^*_{31} only rely on non-180° wall motions. Indeed, 180° walls are not affected by the level of stress. This explanation is consistent with remaining values at 500 MPa. At $E_3 = 0$ (black curves), the remaining χ^*_{33} is 4180 which is 30% of χ^*_{33} ($\sigma_{33} = 2$ MPa) while d^*_{33} is 39 pm/V which is only 1.5% of $d^*_{33}(\sigma_{33} = 2$ MPa).

The evolution of material properties at low stress ($\sigma_{33} < 20$ MPa) is consistent with previous studies [26,74]. The observation of a d^*_{33} and d^*_{31} peak followed by a monotonic decrease above 50 MPa was also reported in [75]. Another recent study made on a single crystal confirms these observations [33]. A similar measurement of d^*_{33} and d^*_{31} under high stress and high electric field can be found in [32,34]. The difference with the present work is that the dependence of the coefficients on the electric field was not shown.

4.3. Material compliance: elastic vs ferroelastic contributions

Fig. 9a and Fig. 9b show the maximum, remanent and minimum values of strain components S_{33} and S_{11} as functions of stress. The gap between the maximum and remanent strains (S_{max} and S_r) increases between 2 and 50 MPa and then continuously decreases until 500 MPa. This evolution is consistent with the observations made in Section 4.2: the electromechanical properties are enhanced in the region 2-100 MPa and deteriorated in the region 100-500 MPa.

The minimum and remanent strains (S_{min} and S_r) converge toward each other when the stress increases. From 300 MPa to 500 MPa, the evolution of S_r and S_{min} is approximately linear. It is assumed that only the elastic contribution remains in this stress range, as the material microstructure is mechanically saturated. This is consistent with a previous study [76] that showed that the compliances s^E_{33} and s^E_{31} of a polarised soft PZT were constant above a stress of 200 MPa. A linear regression between 400 and 500 MPa gives a compliance s_{33} of 7.57 × 10^{-3} GPa^{-1} and a s_{31} of -2.11 × 10^{-3} GPa^{-1}. For comparison purpose, the compliance obtained in the range 300-400 MPa during a pure mechanical test was measured on four samples initially polarised. Similar elastic coefficients were obtained: s_{33} varied from 5.71 × 10^{-3} GPa^{-1} to 6.58 × 10^{-3} GPa^{-1} and s_{31} from 1.76 × 10^{-3} GPa^{-1} to 1.97 × 10^{-3} GPa^{-1}. It shows that the electrical loading applied between each stress level does not affect the elastic coefficients of a stress-saturated PZT, initially polarised.

The ferroelastic contributions S^{ferro}_{33} and S^{ferro}_{11} were then extracted by removing the elastic contributions $S^{elast}_{33} = s_{33}.\sigma_{33}$ and $S^{elast}_{11} = s_{31}.\sigma_{33}$ from the total strain. Results are shown in Fig. 9c and Fig. 9d. The dashed lines schematically illustrate the ferroelastic strain value at the electrical saturation state (maximal ferroelastic elongation) and the mechanical saturation state (maximal ferroelastic contraction). The amplitude between those two lines is representative of the maximum strain amplitude achievable through ferroelastic mechanisms for this material. The ferroelastic strain at the coercive field (orange curve, Fig. 9c and red curve, Fig. 9d) evolves from 2 to 50 MPa and then saturates. The material state at $E = E_c$ is then mechanically saturated above 50 MPa. The ferroelastic strain at zero field (black curves) also changes at low stress and saturates for $\sigma_{33} > 100$ MPa. Thus, $S(E_c)$ is the first point of the S-E loop to saturate. The saturation state then propagates around E_c as long as the stress increases. The mechanical saturation never reaches $S(E_{max})$ since at 500 MPa, a residual ferroelastic strain remains (red curve, Fig. 9c).

The application of a compressive stress tends to increase the achievable ferroelastic strain amplitude. The reason for which it is not observed experimentally – maximum S^{ferro}_{33} is decreasing with the applied stress (Fig. 9c) – is that it would require much higher levels of electric field to overcome the elastic energy saturating the material microstructure.

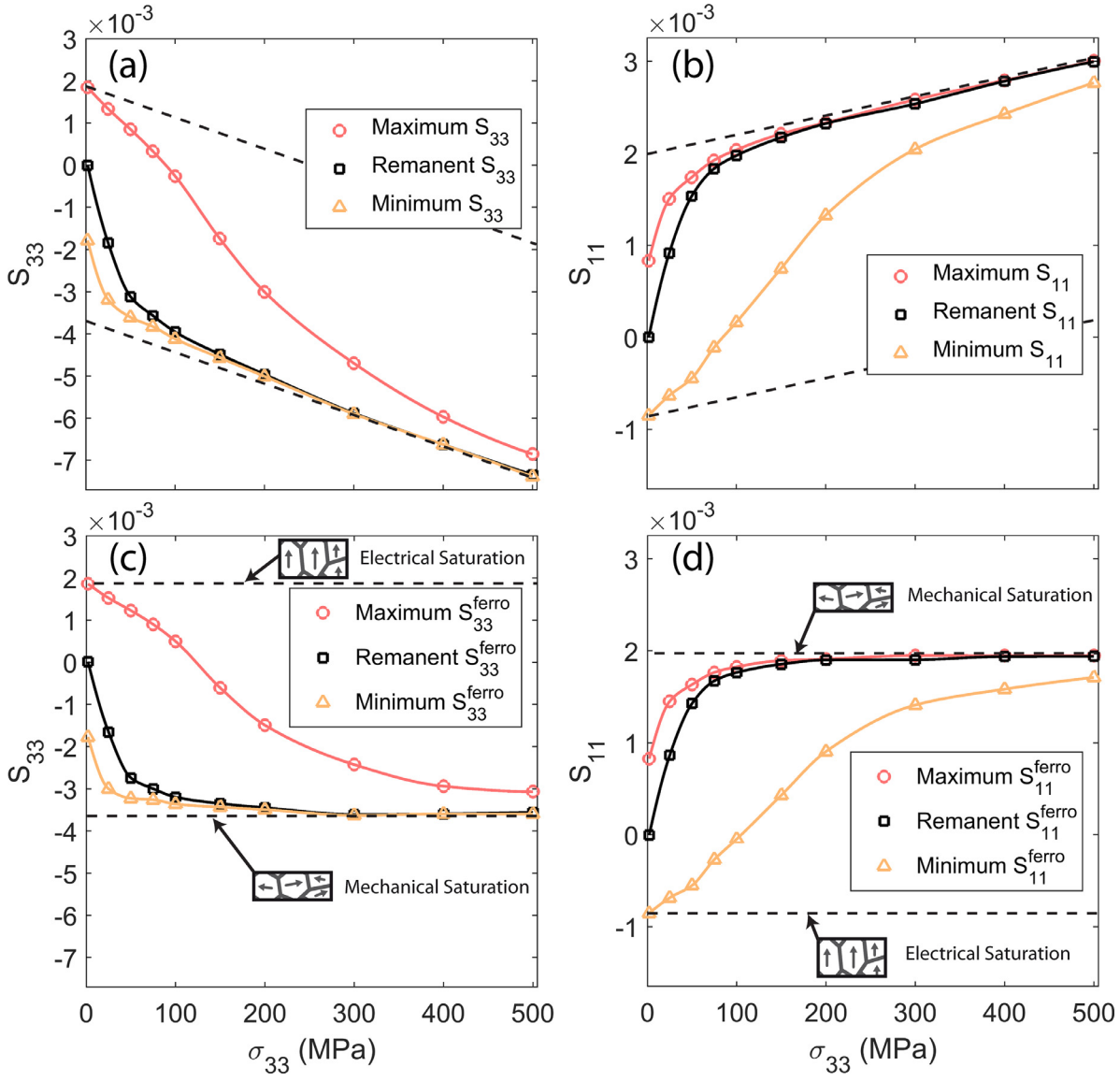

Fig. 9. Minimum, maximum and remanent S_{33} (a) and S_{11} (b) obtained from Fig. 4. Ferroelastic contribution to S_{33} (c) and S_{11} (d) are obtained by removing the elastic contribution in graph (a) and (b). The dashed lines show the higher and lower bound of the ferroelastic strain (electrical and mechanical saturation states). (For interpretation of the references to color in this figure legend, the reader is referred to the web version of this article.)

4.4. Volume variation: piezoelectric vs ferroelastic contributions

It should be noted that contrary to the *S-E* loops, the *P-E* loops are still largely hysteretic above 300 MPa (see Fig. 3). Such a result does not seem to be noted in the literature but can still be observed in [31] and, to a lesser extent, in [21,32,58]. First, among the extrinsic contributions, only non-180° wall motions are responsible for the change in strain. It is thus tempting to conclude that non-180° wall motions are reversible at high stress. This assumption however is not considering the intrinsic effects. For instance, a non-negligible piezoelectric contribution can remain at high stress due to 180° oriented domain. Similarly, the electrostrictive coefficient Q_{33} is ~0.03 m^4/C^2 for PZT [77]. Electrostriction can thus contribute to S_{33} up to 5.10^{-4} at 500 MPa – as the material polarisation reaches 0.13 C/m^2. The intrinsic effects were then evaluated by computing the relative volume variation $\Delta V/V$ from Fig. 4, under transverse isotropy ($S_{22} = S_{11}$) and small strain assumptions:

$$\frac{\Delta V}{V} = S_{33} + 2S_{11} \quad (1)$$

Results are shown in Fig. 10a as a function of the electric field and for different applied stress. Strain values obtained for negative and positive electric fields are averaged. Measurement noise was removed using a moving average filter with a 10 points window (0.5% of the electric field period). The curves exhibit non negligible variations between 2 and 200 MPa. As ferroelastic switching results in an isochoric strain, these volume variations are attributed to intrinsic contributions. The maximum volume change is 2.10^{-4} and occurs at $\sigma_{33} = 2$ MPa and $E = E_{max}$. This point corresponds to the electrical saturation state, where the intrinsic contributions are expected to be maximum. It can be deduced that the intrinsic effects are associated with a volume change of 2.10^{-4} in this material.

Fig. 10b shows, for specific electric fields, the volume variation as a function of stress. Above 200 MPa, the estimated volume variation is of the order of 10^{-5}. It is about one order of magnitude lower compared to the value at low stress. Consequently, it can be assumed that the intrinsic contributions are negligible at high stresses. Domain wall motion is thus presumably the dominant mechanism contributing to strain and polarisation changes.

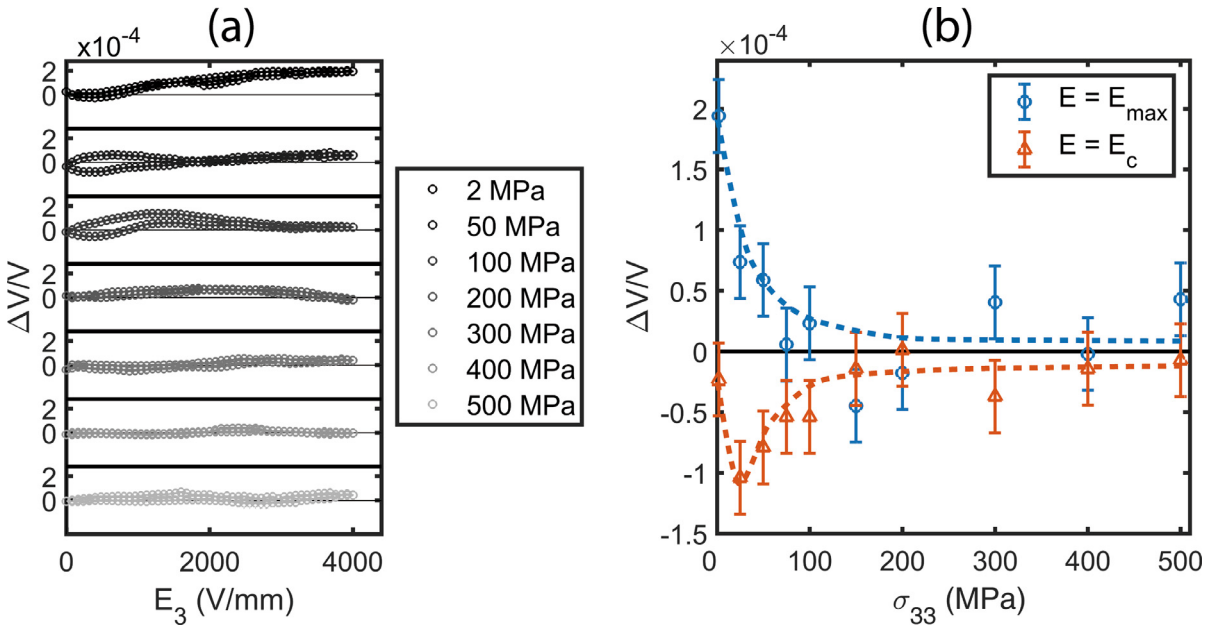

Fig. 10. Relative volume variation $\Delta V/V$ as a function of electric field and stress (a) and relative volume variation $\Delta V/V$ at $E = E_{max}$ and $E = E_c$ as a function of stress (b). Values are computed from Fig. 4 with transverse isotropy hypothesis ($S_{22} = S_{11}$). The elastic contribution is removed. The dash lines in graph (b) are guides for the eye. The error bars represent the error propagated from strain data. (For interpretation of the references to color in this figure legend, the reader is referred to the web version of this article.)

Besides, the S-E curve shows no hysteresis beyond 400 MPa which indicates that non-180° wall motions induced by electric field are reversible. It can further be deduced that the hysteresis seen in the high-stress *P-E* loops comes from 180° wall motions. An explanation is that under large pre-stresses, the amplitude of non-180° wall motion is small due to the intense mechanical pressure. Thus, these walls oscillate between local defects without crossing them. Their motion is then reversible. Contrary to non-180° domain walls, the motion of 180° domain walls does not depend on the level of stress. Therefore, these domain walls cross local defects the same way they do at low stresses.

Another important observation coming from Fig. 10b is that the volume variation at the coercive field exhibits a negative peak in the first region (2 to 100 MPa). This peak reflects the non-monotonic and non-reversible variations of the $\Delta V(E)/V$ curves (Fig. 10a) from 50 to 100 MPa. The origins of these non-linearities are not completely understood. As the apparent (macroscopic) piezoelectric coefficients depend on the polarisation state of the sample (see Fig. 5), a non-linear variation of the piezoelectric response is expected. However, such non-linearity is not present on the 2 MPa curve (Fig. 10a). It is thus difficult to attribute these volume variations to the piezoelectric activity.

Another possible cause is the presence of crystalline phase transitions. Such transitions induced by a combined electromechanical applied field was already observed on PZT with a near-MPB (Morphotropic Phase Boundary) composition [78]. The study showed that a mechanical stress favours the tetragonal phase whereas the electric field favours the rhombohedral phase. It was also observed that the phase transition occurs at the coercive field and that the maximal difference between electric-field-induced phase fractions occurs at a 70 MPa pre-stress. This value is consistent with the peak position observed on the red curve (Fig. 10b, 50 MPa). Since the tested material is mixed-phase, crystalline phase transition around the coercive field and for stresses around 50 MPa is suspected.

5. Conclusion

An original Digital Image Correlation (DIC) technique was used to characterise the strain of a soft PZT under electromechanical loading. This technique was combined with standard polarisation measurements. Results show the *P-E* and *S-E* loops under static stress. The DIC strain field was found to be homogeneous during the electromechanical loading. The accuracy (standard deviation) on the mean strain value was about 3.10^{-5}.

Ferroelectric, dielectric and piezoelectric properties were extracted from the results. The analysis of the data shows that non-180° wall motions are favoured by compressive stress in the range 2-100 MPa. The electromechanical coupling appears to be maximum between 25 and 50 MPa, for electric fields under 500 V/mm.

The ferroelastic contribution was also isolated by removing the elastic contribution, estimated at high stress (300 to 500 MPa). The ferroelastic strain at the coercive field was found to saturate as soon as the stress exceeds 50 MPa. This was explained by the mechanical saturation of the volume fraction of non-180° oriented domains. This saturation state propagates to nearest electric fields when the stress increases and reaches $E_3 = 0$ at $\sigma_{33} = 150$ MPa. It was concluded that this saturation is the cause of the decrease in electromechanical properties, classically observed above 100 MPa for soft PZT.

Another important finding is that DIC can estimate the amplitude of the piezoelectric contribution by analysing the material volume change. This contribution was found to be negligible at 500 MPa. This information allowed the ferroelectric contribution to be isolated. It was deduced that non-180° wall motions are reversible at high stress while 180° wall motions are still significantly affected by dissipative effects. The volume change also appeared to be an indicator for the detection of crystal phase transitions. In the present case, phase transitions presumably occur from 2 to 100 MPa, around the coercive electric field.

DIC opens opportunities for complex studies. Using the material volume change, the technique can further be used to quantitatively

separate the intrinsic and extrinsic contributions to the material behaviour [12]. Such separation is necessary to have, at the macroscopic scale, a view of the different micro-mechanisms contributing to the material behaviour. It is also a convenient macroscopic complementary technique to crystal-scale measurement techniques such as X-Ray diffraction or Atomic Force Microscopy.

Declaration of Competing Interest

The authors declare that they have no known competing financial interests or personal relationships that could have appeared to influence the work reported in this paper.

Acknowledgement

This work was supported by the Automotive Mechatronics Chair, a co-operation between Faurecia, CentraleSupelec, and Esigelec.

The authors wish to thank Professor F. Hild (CNRS, Université Paris-Saclay) for fruitful discussions.

References

[1] P. Hagedorn, J. Wallaschek, Travelling wave ultrasonic motors, part i: working principle and mathematical modelling of the stator, J. Sound Vib. 155 (1992) 31–46.
[2] M. Kurosawa, M. Takahashi, T. Higuchi, Ultrasonic linear motor using surface acoustic waves, IEEE Trans. Ultrason. Ferroelect. Freq. Control 43 (5) (1996) 901–906.
[3] J.A. Fernandez, Y. Perriard, Characteristics, modeling and simulation of a traveling wave ultrasonic linear motor, IEEE Ultrasonics Symposium, 2004, IEEE, 2004.
[4] S. Borodin, J-D. Kim, H-J. Kim, P. Vasiljev, S-J. Yoon, Nano-positioning system using linear ultrasonic motor with "shaking beam", J. Electroceram. 12 (2004) 169–173.
[5] H.F. Vinhais, R.C. Ibrahim, E.C.N. Silva, Simulation of a linear piezoelectric motor by using finite element method, in: *ABCM Symposium Series in Mechatronics*, volume 1, 2004, pp. 697–706. pages.
[6] K. Harmouch, Y. Bernard, L. Daniel, Stator/rotor interface analysis for piezoelectric motors, *9th Exhibition on Smart Actuators and Drive Systems (Actuator 2016)*, pages 459–462, 2016.
[7] N. Snis, U. Simu, S. Johansson, A piezoelectric disc-shaped motor using a quasi-static walking mechanism, J. Micromech. Microeng. 15 (2005) 2230–2234.
[8] A. Suleman, S. Burns, D. Waechter, Design and modeling of an electrostrictive inchworm actuator, Mechatronics 14 (5) (2004) 567–586.
[9] S. Shao, S. Song, N. Chen, M. Xu, Structure and control strategy for a piezoelectric inchworm actuator equipped with mems ridges, Sens. Actuators A 264 (2017) 40–50.
[10] M. Hunstig, Piezoelectric inertia motors - A critical review of history, concepts, design, applications, and perspectives, Actuators 6 (2017) 7.
[11] A. Kappel, B. Gottlieb, T. Schwebel, C. Wallenhauer, Pad - a piezoelectric actuator drive, in: Proc. of the ACTUATOR 2006, 2006, pp. 457–460. pages.
[12] D. Hall, Nonlinearity in piezoelectric ceramics, J. Mater. Sci. 36 (2001) 4575–4601.
[13] K.G. Webber, E. Aulbach, J. Roedel, High temperature blocking force measurements of soft lead zirconate titanate, J. Phys. D-Appl. Phys. 43 (36) (2010) 365401.
[14] A. Pramanick, D. Damjanovic, J.E. Daniels, J.C. Nino, J.L. Jones, Origins of electro-mechanical coupling in polycrystalline ferroelectrics during subcoercive electrical loading, J. Am. Ceram. Soc. 92 (2) (2011) 293–309.
[15] J. Huber, N. Fleck, C.M. Landis, R.M. McMeeking, A constitutive model for ferroelectric polycrystals, J. Mech. Phys. Solids 47 (8) (Aug 1999) 1663–1697.
[16] W. Chen, C.S. Lynch, A micro-electro-mechanical model for polarization switching of ferroelectric materials, Acta Mater. 46 (15) (1998) 5303–5311.
[17] S.P. Alpay, A.L. Roytburd, Thermodynamics of polydomain heterostructures. III. domain stability map, J. Appl. Phys. 83 (9) (1998) 4714–4723.
[18] C.M. Landis, Fully coupled, multi-axial, symmetric constitutive laws for polycrystalline ferroelectric ceramics, J. Mech. Phys. Solids 50 (1) (2002) 127–152.
[19] M. Elhadrouz, T.B. Zineb, E. Patoor, Constitutive law for ferroelastic and ferroelectric piezoceramics, J. Intell. Mater. Syst. Struct. 16 (2005) 221–236.
[20] L. Daniel, D. Hall, P.J. Withers, A multiscale model for reversible ferroelectric behaviour of polycrystalline ceramics, Mech. Mater. 71 (2014) 85–100.
[21] S.A. Zareian Jahromi, *Nonlinear Constitutive Modeling of Piezoelectric Materials*. phdthesis, University of Calgary, 2013.
[22] D. Damjanovic, M. Demartin, The rayleigh law in piezoelectric ceramics, J. Phys. D Appl. Phys. 29 (7) (1996).
[23] C.S. Lynch, The effet of uniaxial stress on the electro-mechanical response of 8/65/35 PLZT, Acta Mater. 44 (10) (1996) 4137–4148.
[24] K.G. Webber, R. Zuo, C.S. Lynch, Ceramic and single-crystal (1-x)PMN-xPT constitutive behavior under combined stress and electric field loading, Acta Mater. 56 (2008) 1219–1227.
[25] D. Damjanovic, Stress and frequency dependence of the direct piezoelectric effect in ferroelectric ceramics, J. Appl. Phys. 82 (1997) 1788.
[26] D. Damjanovic, in: *Hysteresis in piezoelectric and ferroelectric materials*, volume 3, Elsevier, 2006, pp. 337–452. pages.
[27] R. Yimnirun, S. Ananta, A. Ngamjarurojana, S. Wongsaenmai, Uniaxial stress dependence of ferroelectric properties of xPMN-(1-x)PZT ceramic systems, Appl. Phys. A 81 (6) (2005) 1227–1231.
[28] R. Yimnirun, N. Triamnak, M. Unruan, A. Ngamjarurojana, Y. Laosiritaworn, S. Ananta, Ferroelectric properties of $Pb(Zr_{1/2}Ti_{1/2})O_3$-$Pb(Zn_{1/3}Nb_{2/3})O_3$ ceramics under compressive stress, Curr. Appl Phys. (2008).
[29] X. Tan, E. Aulbach, W. Jo, T. Granzow, J. Kling, M. Marsilius, H.-J. Kleebe, J. Rödel, Effect of uniaxial stress on ferroelectric behavior of $(Bi_{1/2}Na_{1/2})TiO_3$-based lead-free piezoelectric ceramics, J. Appl. Phys. 106 (4) (2009) 044107.
[30] S. Patel, A. Chauhan, R. Vaish, Enhanced energy harvesting in commercial ferroelectric materials, Mater. Res. Express 1 (2) (2014) 025504.
[31] P.M. Chaplya, G.P. Carman, Dielectric and piezoelectric response of lead zirconate-lead titanate at high electric and mechanical loads in terms of non-180° domain wall motion, J. Appl. Phys. 90 (2001) 5278.
[32] D. Zhou, M. Kamlah, D. Munz, Uniaxial compressive stress dependence of the high-field dielectric and piezoelectric performance of soft PZT piezoceramics, J. Mater. Res. 19 (3) (2004) 834–842.
[33] F.H. Schader, G.A. Rossetti Jr., J. Luo, K.G. Webber, Piezoelectric and ferroelectric properties of <001>C $Pb(In_{1/2}Nb_{1/2})$ O_3-$Pb(Mg_{1/3}Nb_{2/3})O_3$-$PbTiO_3$ single crystals under combined thermal and mechanical loading, Acta Mater. 126 (2017) 174–181.
[34] D Zhou, M. Kamlah, D. Munz, Effects of uniaxial prestress on the ferroelectric hysteretic response of soft PZT, J. Eur. Ceram. Soc. 25 (4) (2005) 425–432.
[35] B. Wattrisse, A. Chrysochoos, J.-M. Muracciole, M. Némoz-Gaillard, Analysis of strain localization during tensile tests by digital image correlation, Exp. Mech. 41 (1) (2000) 29–39.
[36] V. Tuninetti, G. Gilles, V. Péron-Lührs, A.M. Habraken, Compression test for metal characterization using digital image correlation and inverse modeling, Procedia IUTAM 4 (2012) 206–214.
[37] A. Fathi, J-H. Keller, V. Altstaedt, Full-field shear analyses of sandwich core materials using digital image correlation (DIC), Composites 70 (2015) 156–166.
[38] M. Brabec, R. Lagana, J. Milch, J. Tippner, V. Sebera, Utilization of digital image correlation in determining of both longitudinal shear moduli of wood at single torsion test, Wood Sci. Technol. 51 (1) (2016) 29–45.
[39] A. Farsi, A.D. Pullen, J.P. Latham, J. Bowen, M. Carlsson, E.H. Stitt, M. Marigo, Full deflection profile calculation and young's modulus optimisation for engineered high performance materials, Sci. Rep. 7 (46190) (2017).
[40] B. Pan, D. Wu, Z. Wang, T. Xia, High-temperature digital image correlation method for full-field deformation measurement at 1200°C, Meas. Sci. Technol. 22 (2011) 015701.
[41] L. Chevalier, S. Calloch, F. Hild, Y. Marco, Digital image correlation used to analyze the multiaxial behavior of rubber-like materials, Eur. J. Mech. A. Solids 20 (2001) 169–187.
[42] J-F. Witz, P. Lecomte-Grosbras, A. Morch, C. Martel, F. Lesaffre, M. Brieu, Digital image correlation for large strain, in: M. Sutton, P.L. Reu (Eds.), International Digital Imaging Correlation Society, 2016.
[43] M.W. Nansteel, C.C-T. Chen, Digital image correlation: a measurement tool for the study of explosive effects, Technologies for Homeland Sec, 2009.
[44] L. Fletcher, J. Van-Blitterswyk, F. Pierron, A novel image-based inertial impact test (IBII) for the transverse properties of composites at high strain rates, J. Dyn. Behav. Mater. 5 (2019) 65–92.
[45] M.H. Malakooti, H.A. Sodano, Direct measurement of piezoelectric shear coefficient, J. Appl. Phys. 113 (2013) 214106.
[46] M.H. Malakooti, H.A. Sodano, Noncontact and simultaneous measurement of the d33 and d31 piezoelectric strain coefficients, Appl. Phys. Lett. 102 (2013) 061901.
[47] D. Chen, M. Kamlah, Deformation in lead zirconate titanate ceramics under large signal electric field loading measured by digital image correlation, Rev. Sci. Instrum. 86 (2015) 113707.
[48] D. Chen, E. Carter, M. Kamlah, Deformation behavior of lead zirconate titanate ceramics under uniaxial compression measured by the digital image correlation method, Smart Mater. Struct. 25 (2016) 097001.
[49] V. Segouin, M. Domenjoud, Y. Bernard, L. Daniel, Mechanics-aided digital image correlation for the investigation of piezoelectric and ferroelectric behaviour of a soft PZT, J. Eur. Ceram. Soc. 39 (6) (2019) 2091–2102.
[50] A.M. Glazer, P. Groves, D.T. Smith, Automatic sampling circuit for ferroelectric hysteresis loops, J. Phys. E Sci. Instrum. 17 (2) (1984) 95–97.
[51] M. Stewart, M.G. Cain, D. Hall, Ferroelectric Hysteresis Measurement & Analysis, National Physical Laboratory and University of Manchester, 1999 report (no.cmmt/a.152) issn 1368-6550; edition.
[52] V. Segouin, M. Domenjoud, Y. Bernard, D. Daniel, Development of a 2d DIC experimental tool for piezoelectric strains measurements, in: International Digital Imaging Correlation Society, Springer International Publishing, 2017, pp. 45–50. pages.
[53] Z. Tomicevc, F. Hild, S. Roux, Mechanics-aided digital image correlation, J. Strain Anal. Eng. Des. 48 (5) (2013) 330–343.
[54] D. Munz, T. Fett, Ceramics, 3, Springer Berlin Heidelberg, 1999.

[55] D. Zhou. *Experimental Investigation of Non-linear Constitutive Behavior of PZT Piezoceramics*. PhD thesis, der Fakultät für Maschinenbau der Universität Karlsruhe (TH), 2003.
[56] M.A. Sutton, J.H. Yan, V. Tiwari, H.W. Schreier, J.J. Orteu, The effect of out-of-plane motion on 2D and 3D digital image correlation measurements, Opt. Lasers Eng. 46 (2008) (2008) 746–757.
[57] R. Yimnirun, S. Wongsaenmai, Y. Laosiritaworn, S. Ananta, Uniaxial stress dependence and scaling behavior of dynamic hysteresis responses in soft PZT ceramics, 2006 IEEE International Symposium on the Applications of Ferroelectrics, 2006.
[58] A. Skaliukh. *About Mathematical Models of Irreversible Polarization Processes of a Ferroelectric and Ferroelastic Polycrystals*, chapter Chapter 4. 2018.
[59] S. Li, W. Cao, L.E. Cross, The extrinsic nature of nonlinear behavior observed in lead zirconate titanate ferroelectric ceramic, J. Appl. Phys. 69 (1991) 7219.
[60] Q.M. Zhang, H. Wang, N. Kim, L.E. Cross, Direct evaluation of domain wall and intrinsic contributions to the dielectric and piezoelectric response and their temperature dependence on lead zirconate titanate ceramics, J. Appl. Phys. 75 (1994) 454.
[61] D. Damjanovic, Contributions to the piezoelectric effect in ferroelectric single crystals and ceramics, J. Am. Ceram. Soc. 88 (10) (oct 2005) 2663–2676.
[62] D. Berlincourt, H.H.A. Krueger, Domain processes in lead titanate zirconate and barium titanate ceramics, J. Appl. Phys. 30 (11) (nov 1959) 1804–1810.
[63] H.H.A. Krueger, Stress sensitivity of piezoelectric ceramics: Part 3. sensitivity to compressive stress perpendicular to the polar axis, J. Acoust. Soc. Am. 43 (3) (Mar. 1968) 583–591.
[64] H. Cao, A.G. Evans, Nonlinear deformation of ferroelectric ceramics, J. Am. Ceram. Soc. 76 (4) (Apr 1993) 890–896.
[65] M. Kamlah, Ferroelectric and ferroelastic piezoceramics modeling of electromechanical hysteresis phenomena, Continuum. Mech. Thermodyn. 13 (4) (aug 2001) 219–268.
[66] D.A. Hall, A. Steuwer, B. Cherdhirunkorn, T. Mori, P.J. Withers, Analysis of elastic strain and crystallographic texture in poled rhombohedral PZT ceramics, Acta Mater. 54 (11) (jun 2006) 3075–3083.
[67] F.X. Li, R.K.N.D. Rajapakse, Analytical saturated domain orientation textures and electromechanical properties of ferroelectric ceramics due to electric/mechanical poling, J. Appl. Phys. 101 (054110) (2007).
[68] Julius Adams Stratton, Electromagnetic Theory, Mcgraw Hill Book Company, 1941.
[69] A. L. Kholkin, N.A. Pertsev, and A. V. Goltsev. Piezoelectricity and crystal symmetry. In *Piezoelectric and Acoustic Materials for Transducer Applications*, chapter Chapter 2, pages 17–38. Springer US, 2008.
[70] N. Wongdamnern, N. Triamnak, A. Ngamjarurojana, Y. Laosiritaworn, S. Ananta, R. Yimnirun, Comparative studies of dynamic hysteresis responses in hard and soft pzt ceramics, Ceram. Int. 34 (2008) 731–734.
[71] X. Wu, X. Lu, A. Chen, Y. Yin, J. Ma, W. Li, Y. Kan, D. Qian, J. Zhu, Stress effects on ferroelectric and fatigue properties of Nd- and La-doped $Bi_4Ti_3O_{12}$ thin films, Appl. Phys. Lett. 86 (2005) 092904.
[72] B. Peng, Z. Yue, Effect of uniaxial compressive stress on the partially fatigued soft lead zirconate titanate piezoelectric ceramics, Key Eng. Mater. 602-603 (2014) 817–821.
[73] L. Daniel, D.A. Hall, J. Koruza, K.G. Webber, A. King, P.J. Withers, Revisiting the blocking force test on ferroelectric ceramics using high energy x-ray diffraction, J. Appl. Phys. 117 (2015) 174104.
[74] D. Damjanovic, Ferroelectric, dielectric and piezoelectric properties of ferroelectric thin films and ceramics, Rep. Prog. Phys. 61 (1998) 1267–1324.
[75] R. Dittmer, K.G. Webber, E. Aulbach, J. Wook, X. Tan, J. Rödel, Optimal working regime of lead-zirconate-titanate for actuation applications, Sens. Actuators, A 189 (2013) 187–194.
[76] Q.D. Liu, J.E. Huber, State dependent linear moduli in ferroelectrics, Int. J. Solids Struct. 44 (2007) 5635–5650.
[77] G. Zorn, W. Wersing, H. Göbel, Electrostrictive tensor components of PZT-ceramics measured by X-ray diffraction, Japan. J. Appl. Phys. 24 (1985) 721.
[78] G. Esteves, C.M. Francher, S. Röhrig, G.A. Maier, J.L. Jones, M. Deluca, Electric–field-induced structural changes in multilayer piezoelectric actuators during electrical and mechanical loading, Acta Mater. 132 (2017) 9.